processes

MDPI

Article

Thermal Performance and Entropy Generation of Unsteady Natural Convection in a Trapezoid-Shaped Cavity

Md. Mahafujur Rahaman [1,2,*], Sidhartha Bhowmick [1] and Suvash C. Saha [3,*]

[1] Department of Mathematics, Jagannath University, Dhaka 1100, Bangladesh; sidharthabhowmick@yahoo.com
[2] Department of Computer Science and Engineering, Z. H. Sikder University of Science and Technology, Shariatpur 8024, Bangladesh
[3] School of Mechanical and Mechatronic Engineering, University of Technology Sydney, Ultimo, NWS 2007, Australia
* Correspondence: mahfuz0809@gmail.com (M.M.R.); suvash.saha@uts.edu.au (S.C.S.)

Abstract: In this study, a numerical investigation of unsteady natural convection heat transfer (HT) and entropy generation (EG) is performed within a trapezoid-shaped cavity containing thermally stratified water. The cavity's bottom wall is heated, the sloped walls are thermally stratified, and the top wall is cooled. The finite volume (FV) method is employed to solve the governing equations. This study uses a Prandtl number (Pr) of 7.01 for water, an aspect ratio (*AR*) of 0.5, and Rayleigh numbers (Ra) varying between 10 and 10^6. To examine the flow behavior within the cavity, various relevant parameters are determined for different Ra values. These parameters include streamline and isotherm contours, temperature time series, limit point and limit cycle analysis, average Nusselt number (Nu) at the heated walls, average entropy generation (E_{avg}), and average Bejan number (Be_{avg}). It is found that the flow transitions from a steady symmetrical state to a chaotic state as the Ra value increases. During this transition, three bifurcations occur. The first is a pitchfork bifurcation between Rayleigh numbers of 9×10^4 and 10^5, followed by a Hopf bifurcation between Rayleigh numbers of 10^5 and 2×10^5. Finally, another bifurcation occurs, shifting the flow from periodic to chaotic between Rayleigh numbers of 4×10^5 and 5×10^5. The present study shows an increase in E_{avg} of 94.97% between Rayleigh numbers of 10^3 and 10^6, while the rate of increase in Nu is 81.13%. The findings from this study will enhance understanding of the fluid flow phenomena in a trapezoid-shaped cavity filled with stratified water. The current numerical results are compared and validated against previously published numerical and experimental data.

Keywords: natural convection; entropy generation; heat transfer; stratified water; bifurcations

check for updates

Academic Editors: Sergio Alejandro Martínez Delgadillo and Alejandro Alonzo-Garcia

Received: 11 February 2025
Revised: 12 March 2025
Accepted: 19 March 2025
Published: 20 March 2025

Citation: Rahaman, M.M.; Bhowmick, S.; Saha, S.C. Thermal Performance and Entropy Generation of Unsteady Natural Convection in a Trapezoid-Shaped Cavity. *Processes* **2025**, *13*, 921. https://doi.org/10.3390/pr13030921

Copyright: © 2025 by the authors. Licensee MDPI, Basel, Switzerland. This article is an open access article distributed under the terms and conditions of the Creative Commons Attribution (CC BY) license (https://creativecommons.org/licenses/by/4.0/).

1. Introduction

Natural convection (NC) occurs due to temperature variations within a fluid occurring without the influence of external forces. This phenomenon is commonly found in various fields, including solar collectors [1], building heating and ventilation [2], heat exchangers [3], electronic cooling [4], energy storage [5], and others [6]. Natural convection has been extensively studied in numerous cavity geometries with multiple boundary conditions and different numerical methods to investigate thermal behavior and fluid flow. Saha [7] discovered fluid flow and heat transport within a triangular cavity due to abrupt heating on the sloped sides using an advanced scaling approach. Bhowmick et al. [8] studied the shift of fluid flow from a steady to a chaotic state inside of a V-shaped enclosure with a heated base. Wang et al. [9] conducted experiments on NC in a V-shaped cavity to investigate the

fluid behavior and HT phenomena. Later, Bhowmick et al. [10] conducted a numerical analysis of NC within a V-shaped cavity with differential heating.

In natural environments, such as the atmosphere and the ocean, as well as in numerous industrial settings, HT mechanisms frequently occur via NC in stratified media. Despite its substantial influence on HT processes, there are only a few studies in the literature that focus on this phenomenon. Eichhorn and his team [11–14] carried out pioneering research on natural convection HT in fluids with constant thermal properties, proposing numerous solutions to predict HT from the vertical plate in stratified fluids. Angirasa and Srinivasan [15] investigated NC on an isothermal surface in a surrounding fluid within a thermally stratified porous medium, exploring the effects of the HT rate on the intensities of thermal stratification. Tripathi and Nath [16] employed numerical analysis to study NC in a stratified fluid near a vertical isothermal wall. Further research by Hossain et al. [17], Lin et al. [18], and Shapiro and Fedorovich [19,20] examined the effects of stratification on NC in several geometries, such as semi-infinite plates, vertical circular cones, and infinite vertical plates. Their research provided analytical solutions for Pr equal to one, as well as for sudden temperature variations and fluctuations in heat flux. Shapiro and Fedorovich [21] prolonged their exploration to analysis of how the Pr affects convection in stratified fluids along individual vertical plates using both numerical and analytical methods.

In engineering settings, natural convection (NC) flows are generally unsteady, leading to significant studies on the transition of these flows within enclosures dealing with abrupt cooling and heating. Patterson and Imberger [22] provided detailed insights into the unsteady behavior of NC inside of a rectangular enclosure, highlighting the evolution of flow patterns, the role of thermal stratification, and the importance of dimensionless parameters like the Ra in characterizing the flow and HT. Subsequently, Kuhn and Oosthuizen [23] examined the dynamics of HT and flow within a rectangular cavity subjected to differential heating. Lei et al. [24] used a shadowgraph technique to visualize the unsteady flow dynamics in an isosceles triangular cavity. Ma and Xu [25] investigated the enhancement of convective flow and HT in a differentially heated enclosure at higher Ra, focusing on the dependence of oscillation frequency and HT efficiency within the cavity on the Rayleigh number. They also studied the effects of placing a fin at various positions along the sidewall, providing insights into how these factors influence the system's overall thermal performance. Xu et al. [26] examined the shift of NC flows generated by a conducting fin, aiming to measure the variances in flow characteristics between cases involving an adiabatic fin and a conducting fin. Their study highlighted how the thermal conductivity of the fin influences the flow patterns as well as HT efficiency inside of the cavity.

In numerous engineering applications, particularly in geophysical environments where enclosure geometry is irregular or incorporates inclined walls, conventional square, triangular, or rectangular enclosures are often insufficient for accurate modeling and analysis. Due to the presence of inclined walls, trapezoidal enclosures present a greater challenge for studying NC compared to other intricate cavity geometries, such as elliptical [27,28], concentric [29,30], eccentric [31,32], and titled cavities [33]. The construction of computational meshes and the development of numerical codes for trapezoidal geometry demands precise and meticulous attention due to their complexity. Pioneering studies on NC heat transfer in enclosed trapezoidal cavities, offering both analytical and experimental results, were conducted by Iyican et al. [34,35]. Similar results were stated by Lam et al. [36] in a trapezoidal cavity for a heated base wall, a slanted cold top wall, as well as two perpendicular insulated walls. Lee [37] studied a non-rectangular enclosure with aspect ratios ranging from three to six, focusing on the effects of Ra, Pr, and varying sloped angles. The findings indicate that the Pr, Ra, and sloped angle of the cavity are critical factors significantly affecting HT and fluid flow. Perić [38] examined the same problem previously

investigated by Lee [37] and noted that the outcomes varied both quantitatively and qualitatively compared to Lee's outcomes. Kuyper and Hoogendoorn [39] further discovered the impact of the sloped angle of isothermal walls on flow dynamics and the effects of Ra on NC heat transfer inside of a trapezoidal cavity.

Moukalled and Darwish [40] investigated NC flows inside of a partitioned trapezoidal cavity featuring a baffle attached to the base wall. They discovered that raising the altitude of the baffle and the Prandtl number caused a decrease in HT. Subsequently, Moukalled and Darwish [41] examined NC flows within the same cavity with a baffle pinned at top tilled wall. In a later study, Moukalled and Darwish [42] explored NC in a trapezoidal cavity featuring two offset baffles. Natarajan et al. [43,44] investigated NC flow within a trapezoidal cavity, characterized by a uniformly heated base and vertical surfaces that were either linearly cooled or heated. Basak et al. [45] extended this study by examining NC in a trapezoidal enclosure under boundary conditions like those of Natarajan et al. [43,44] but with varying sloping angles for the sidewalls. Additionally, Basak et al. [46] examined NC in a trapezoidal cavity with both non-uniformly and uniformly heated base surfaces, an insulated upper surface, and sloped isothermal side surfaces. Their findings revealed that despite uneven heating of the bottom walls, the HT rate remained relatively unchanged. Furthermore, Lasfer et al. [47] investigated the steady NC flow of air within a trapezoidal cavity with a heated sloped left wall, a cooled perpendicular right wall, as well as insulated flat horizontal walls. Recently, Rahaman et al. [48–52] thoroughly investigated NC heat transfer inside of a trapezoidal cavity for several fluid properties and boundary conditions.

In the above literature, it appears that researchers have primarily considered the first law of thermodynamics to investigate fluid flow and thermal behavior using numerical and experimental models. However, Bejan [53] employed the second law of thermodynamics to assess the irreversibility involved in basic HT processes. Bejan [54] initially introduced the notion of entropy generation (EG) minimization across diverse transport processes to enhance energy efficiency by examining the reduction in available energy through EG. Lately, there has been a significant increase in the utilization of the EG minimization method as a method of thermodynamic optimization for various thermal systems [55,56]. In [57,58], researchers investigated the impact of EG on the benchmark problem of NC in a rectangular cavity with vertically heated walls and horizontally adiabatic walls. Additionally, in [59–62], researchers explored the influence of irreversibility related to HT and fluid friction (FF) in their investigations of various thermal systems within a porous medium. Recently, Rahaman et al. [63] examined the impact of the aspect ratio on NC, HT, and EG within a trapezoidal cavity. Their findings revealed that as the aspect ratio rises, the cavity's thermal performance decreases. Findings of the past studies on the trapezoidal cavity have been summarized and presented in Table 1.

The analysis of the literature reveals that several investigations have been conducted to study NC, HT phenomena, and EG analysis using various methods in different cavities. As far as we know, unsteady NC heat transfer and EG in a trapezoid-shaped cavity containing thermally stratified water and featuring a heated bottom wall, stratified sloped walls, and a cooled top wall have not been extensively investigated previously. To fill this gap, the current study adopts a novel approach to explore the fluid flow, HT, and EG within the cavity. To validate the model's accuracy, a couple of comparisons are made with the experimental findings [24,35] and the numerical results presented in [47].

Table 1. Key findings of past studies on the trapezoidal cavity.

References	Parameters	Key Findings
Iyican et al. [34]	φ = 0–180° Pr = 0.71	Described how the flow structures and HT are influenced by the inclination of the walls and the Ra.
Iyican et al. [35]	φ = 0–180°	Developed correlations for the Nu as a function of the Ra. These correlations agree with the findings of the earlier analytical study.
Lam et al. [36]	φ = 0–25° Pr = 0.71	Examined the effect of the Ra and the sloped angle on fluid flow and HT.
Lee [37]	AR = 3–6 φ = 22.5°, 45°, 77.5° Pr = 0.001–100	Investigated the effect of the Ra, Pr, and sloped angle on fluid flow and HT.
Perić [38]	φ = 0°, 90°, 180°, 270° Pr = 0.7	Analyzed Lee's results and observed that the outcomes differed both quantitatively and qualitatively.
Kuyper and Hoogendoorn [39]	φ = 0–45° Pr = 0.71	Discovered the impact of the sloped angle and Ra on fluid flow and HT.
Moukalled and Darwish [40,41]	AR = 0.5 Pr = 0.7, 10, 130	Revealed the influence of the baffle position and the Pr on fluid flow and HT.
Moukalled and Darwish [42]	AR = 0.5 Pr = 0.7, 10, 130	Discovered the effect of two offset baffles and the Pr on fluid flow and HT.
Natarajan et al. [43,44]	φ = 30° Pr = 0.7–100	Revealed that the effect of the Pr on HT is more significant for Pr values between 0.07 and 0.7 than for values between 10 and 100.
Basak et al. [45]	φ = 45°, 30°, 0° Pr = 0.026–1000	Demonstrated that the HT rate is higher for uniform heating of the bottom wall compared to non-uniform heating of the bottom wall.
Basak et al. [46]	φ = 0–45° Pr = 0.7–100	Discovered that the HT rate remained unchanged due to the uneven heating of the bottom walls.
Lasfer et al. [47]	AR = 0.5, 1.0, 1.5 φ = 60°–120° Pr = 0.71	Showed that the flow and HT depend significantly on the sloped angle, AR, and thermal strength.
Rahaman et al. [48,49]	AR = 0.5 Pr = 0.71	Described the flow transition from a steady to a chaotic state with a higher Ra and demonstrated how different Ra values influence the flow and heat transfer characteristics.
Rahaman et al. [50]	AR = 0.5 Pr = 0.71	Provided detailed insights into fluid flow behavior, including vortex formation, oscillatory patterns, and chaotic flow.
Rahaman et al. [51]	AR = 1.0 Pr = 0.71	Discovered a series of bifurcations involved in the shifting of convective flows from a symmetric steady state to an unsteady state.
Rahaman et al. [52]	AR = 0.2 Pr = 0.71	Revealed fluid flow and HT behavior within the cavity for lower AR.
Rahaman et al. [63]	AR = 0.2, 0.5, 1.0 Pr = 0.71	Studied the critical Ra value for each AR in the transition from a symmetric to a chaotic state and illustrated how thermal performance depends on AR.
Current study	AR = 0.5 Pr = 7.01	Considered a Pr of 7.01 to investigate fluid flow, HT rates, and the transition from a steady to a chaotic state. Also demonstrated how the energy efficiency and environmental impact depend on the Ra.

2. Problem Formulations

The physical domain, including the appropriate boundary conditions, is depicted in Figure 1. The cavity has a vertical height of H and a horizontal length of $2L$, with $L = 2H$, resulting in an aspect ratio (AR) of $H/L = 0.5$. To avoid singularities at the corners between the tilled and top walls, small sections at the upper corners (4% of L) were omitted. The thermal condition at the truncated tiny tips is defined as adiabatic. Previous investigations [7,64] have demonstrated that slight geometric modifications have negligible effects on NC flow and HT. To validate this negligible effect on NC flow, isotherm contours for both truncated and non-truncated geometries were presented in the author's previous study (see Ref. [49], Figure 3). In that study, the numerical results were compared with those of Basak et al. [45], who used a non-truncated geometry. Initially, the water within the cavity is thermally stratified, with the lowest temperature, θ_c, at the top of the cavity, and the maximum temperature, θ_h, at the bottom. The sloped walls are thermally stratified, with temperatures ranging from the maximum near the bottom wall to the lowermost adjacent to the top wall. Thermo-physical properties of the stratified water are presented in Table 2. All of the boundary walls are rigid and subject to a non-slip condition.

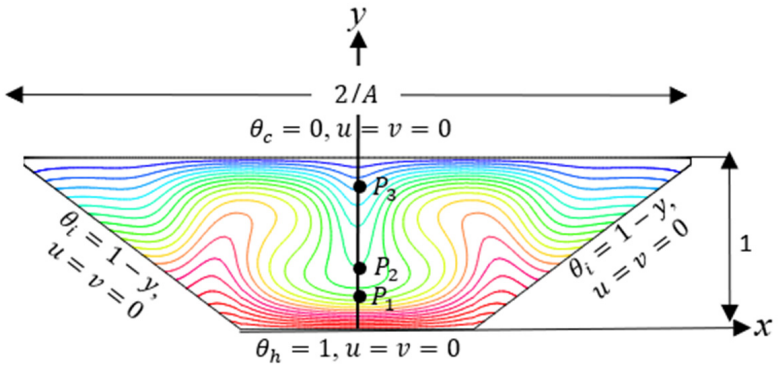

Figure 1. Schematic of physical domain and dimensionless boundary conditions with result monitoring points P_1 (0, 0.27), P_2 (0, 0.40), and P_3 (0, 0.67), which are utilized in the subsequent figures.

In the trapezoidal cavity, NC flow of stratified water is supposed. The dimensional governing equations, with Boussinesq approximation, govern the development of NC flow within the cavity as

$$\frac{\partial U}{\partial X} + \frac{\partial V}{\partial Y} = 0, \tag{1}$$

$$\frac{\partial U}{\partial t} + U\frac{\partial U}{\partial X} + V\frac{\partial U}{\partial Y} = -\frac{1}{\rho}\frac{\partial P}{\partial X} + \nu\left(\frac{\partial^2 U}{\partial X^2} + \frac{\partial^2 U}{\partial Y^2}\right), \tag{2}$$

$$\frac{\partial V}{\partial t} + U\frac{\partial V}{\partial X} + V\frac{\partial V}{\partial Y} = -\frac{1}{\rho}\frac{\partial P}{\partial Y} + \nu\left(\frac{\partial^2 V}{\partial X^2} + \frac{\partial^2 V}{\partial Y^2}\right) + g\beta(T - T_0), \tag{3}$$

$$\frac{\partial T}{\partial t} + U\frac{\partial T}{\partial X} + V\frac{\partial T}{\partial Y} = \kappa\left(\frac{\partial^2 T}{\partial X^2} + \frac{\partial^2 T}{\partial Y^2}\right). \tag{4}$$

The following are the normalized variables that were utilized:

$$x = \frac{X}{H},\ y = \frac{Y}{H\sqrt{\mathrm{Ra}}},\ u = \frac{UH}{\kappa\sqrt{\mathrm{Ra}}},\ v = \frac{VH}{\kappa\sqrt{\mathrm{Ra}}},\ p = \frac{PH^2}{\rho\kappa^2\mathrm{Ra}},\ \theta = \frac{T - T_\infty}{T_h - T_c},\ \tau = \frac{t\kappa\sqrt{\mathrm{Ra}}}{H^2}. \tag{5}$$

The three parameters, such as AR, Pr, and Ra [65], influence the NC flow inside of the cavity, and they can be formulated as follows:

$$Ra = \frac{g\beta(T_h - T_c)H^3}{\nu\kappa},\ Pr = \frac{\nu}{\kappa},\ A = \frac{H}{\mathrm{L}}. \tag{6}$$

Equations (1) to (4) become, after adding the normalized variables, as follows:

$$\frac{\partial u}{\partial x} + \frac{\partial v}{\partial y} = 0, \tag{7}$$

$$\frac{\partial u}{\partial \tau} + u\frac{\partial u}{\partial x} + v\frac{\partial u}{\partial y} = -\frac{\partial p}{\partial x} + \frac{Pr}{\sqrt{\mathrm{Ra}}}\left(\frac{\partial^2 u}{\partial x^2} + \frac{\partial^2 u}{\partial y^2}\right), \tag{8}$$

$$\frac{\partial v}{\partial \tau} + u\frac{\partial v}{\partial x} + v\frac{\partial v}{\partial y} = -\frac{\partial p}{\partial y} + \frac{Pr}{\sqrt{\mathrm{Ra}}}\left(\frac{\partial^2 v}{\partial x^2} + \frac{\partial^2 v}{\partial y^2}\right) + Pr\theta, \tag{9}$$

$$\frac{\partial \theta}{\partial \tau} + u\frac{\partial \theta}{\partial x} + v\frac{\partial \theta}{\partial y} = \frac{1}{\sqrt{\mathrm{Ra}}}\left(\frac{\partial^2 \theta}{\partial x^2} + \frac{\partial^2 \theta}{\partial y^2}\right). \tag{10}$$

Normalized boundary conditions are as follows:

$$\begin{cases} \theta_c = u = v = 0, \text{ at the top wall} \\ \theta_h = 1, u = v = 0, \text{ at the bottom wall} \\ \theta_i = 1 - y, u = v = 0, \text{ at the inclined walls.} \end{cases} \tag{11}$$

The average Nusselt number at the horizontal as well as the sloped walls is defined as follows (for details, refer to Rahaman et al. [65]):

$$\mathrm{Nu} = \frac{1}{l}\int_0^1 \frac{\partial \theta}{\partial y} dx \text{ and } \mathrm{Nu} = \frac{1}{l}\int_0^1 \frac{\partial \theta}{\partial n} ds. \tag{12}$$

In an NC system, irreversibility is caused by HT and fluid friction (FF). According to the linear transport theory (refer to Bejan [54] for further details), the normalized local entropy generation (EG) due to HT and FF can be written as

$$E_\theta = \left(\frac{\partial \theta}{\partial x}\right)^2 + \left(\frac{\partial \theta}{\partial y}\right)^2. \tag{13}$$

$$E_f = \psi\left[2\left\{\left(\frac{\partial u}{\partial x}\right)^2 + \left(\frac{\partial v}{\partial y}\right)^2\right\} + \left(\frac{\partial u}{\partial y} + \frac{\partial v}{\partial x}\right)^2\right]. \tag{14}$$

where E_θ and E_f represent the local EG due to HT and FF, respectively. In Equation (14), ψ is denoted as the irreversibility distribution ratio, defined as

$$\psi = \frac{\mu T_\infty}{k}\left(\frac{\kappa}{L\Delta T}\right)^2. \tag{15}$$

In the present study, ψ is chosen as 10^{-3}; for more details, refer to Varol et al. [59].

The local entropy generation inside of the enclosure, represented by E_l, is the sum of Equations (13) and (14), as follows:

$$E_l = E_\theta + E_f\ . \tag{16}$$

The local Bejan number (Be_l), average entropy generation (E_{avg}), and the average Bejan number (Be_{avg}) are defined as follows (for details, refer to Rahaman et al. [63]):

$$Be_l = \frac{E_\theta}{E_\theta + E_f}\ . \tag{17}$$

$$E_{avg} = \frac{\int_0^1 \int_0^1 E_l\, dx\, dy}{\int_0^1 \int_0^1 dx\, dy}. \tag{18}$$

$$Be_{avg} = \frac{\int_0^1 \int_0^1 Be_l \, dx \, dy}{\int_0^1 \int_0^1 dx \, dy}. \tag{19}$$

The ecological coefficient of performance (ECOP) is defined as follows (for further details, refer to Rahaman et al. [63]):

$$\text{ECOP} = \frac{\text{Nu}}{E_{avg}}. \tag{20}$$

Table 2. Thermo-physical properties of the working fluid (for further details, refer to Rahaman et al. [65]).

Property (Unit)	Water
k (W/m K)	0.566
ρ (kg/m^3)	998.4
C_p (J/kg K)	4182
μ (kg/m s)	9.4748×10^{-4}
β (1/K)	3.109×10^{-4}

3. Numerical Model

The governing Equations (7) to (10), and their respective boundary conditions in Equation (11), are discretized using the finite volume (FV) method (for details, refer to Rahaman et al. [49,50]). In this research, Fluent 17.0, which is based on the FV method, is used to simulate the NC flow inside of a trapezoid-shaped cavity. The SIMPLE scheme is applied for the pressure–velocity coupling. The diffusion terms are discretized utilizing a second-order central differencing approach, although the advection terms are discretized using a third-order accurate QUICK scheme, as described by Patterson and Armfield [22] and Saha et al. [64]. Additionally, a second-order implicit time-marching approach is used for the transient term. A non-uniform rectangular grid arrangement is employed in this study, and under-relaxation factors are applied to iterate the discretized equations (for further details, refer to Saha and Gu [66]). A convergence criterion of 10^{-5} is implemented for the continuity, momentum, and energy equations.

4. Grid and Time Step Dependent Tests

The accuracy and stability of numerical simulations are largely dependent on the grid size used within the computational domain. To evaluate the sensitivity of the grid and time step, a comparison was conducted at the highest Ra based on the assumption that the mesh and time step selected for this maximum Ra would also be appropriate for cases with lower Ra. Three symmetrical grids of 225 × 75, 300 × 100, and 375 × 125 and two time steps of 0.01 and 0.005 were carefully chosen for the comparison. In Figure 2, calculate the temperature time series at position P_1 within the cavity, where the flow is the most unstable. For all grids and time steps, the temperature time series coincides initially and varies during the initial transitional phase but closely coincides through the fully developed stage. From this result, we conclude that all of the grid configurations employed were sufficiently acceptable to accurately resolve the flow. As a result, a grid size of 300 × 100 and a time step of 0.01 were selected for the numerical simulations.

In this study, the dimensionless dissipative time scale is calculated based on the following relation (refer to [8] for more details):

$$\lambda_k = \left(32\pi\sqrt{2}\right)^{1/4} \left(\text{Ra}/\text{Pr}\right)^{-3/8}. \tag{21}$$

Here, λ_k is 0.0403 for Ra = 10^6; therefore, the dimensionless time steps of 0.01 and 0.005 are chosen for the comparison.

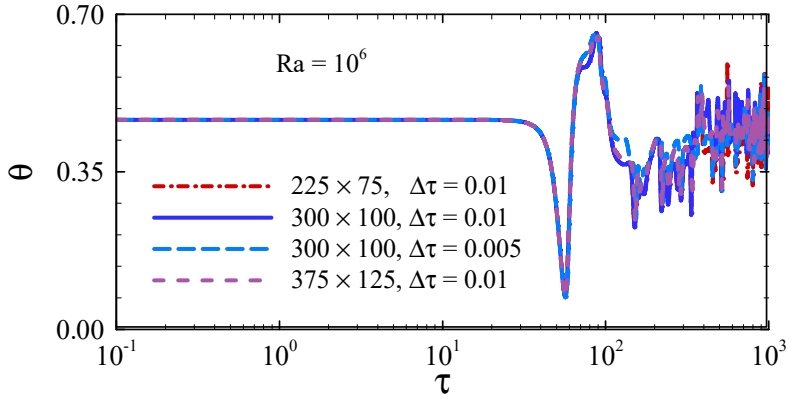

Figure 2. Temperature time series at P_1 (0, 0.27) for Ra = 10^6 with different grids as well as time steps.

5. Model Validation

To validate the present model and its outcomes, the results are compared with experimental findings from Lei et al. [24] and Iyican et al. [35], as well as numerical results from Lasfer et al. [47]. A qualitative validation of the isotherm is illustrated in Figure 3. For this comparison, the fluid's initial temperature of T_∞ = 293.5 K is used, along with a Prandtl number of 7.06 for water. A Rayleigh number of 1.67 × 10^6 is obtained by setting the temperatures to T_c = 289.5 K and T_h = 297.5 K. This comparison demonstrates an outstanding level of agreement.

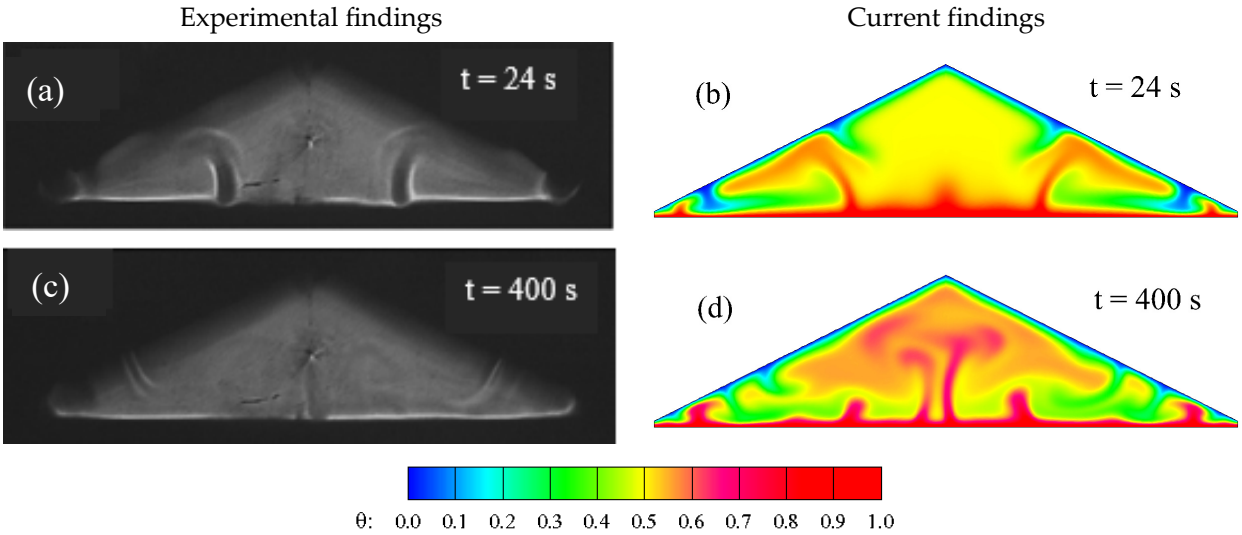

Figure 3. Qualitative comparison of present results (**b**,**d**) with experimental findings (**a**,**c**) for isotherms, considering Ra = 1.67 × 10^6.

Additionally, a quantitative validation of the average Nusselt number (Nu) is presented in Figure 4. This comparison is based on dimensionless parameters, with a Pr of 0.7, Ra spanning from 10^3 and 10^7, and a slope angle of 90°. The current results show excellent agreement with both the numerical and experimental findings, suggesting that the present solver is both practical and efficient for supporting this work.

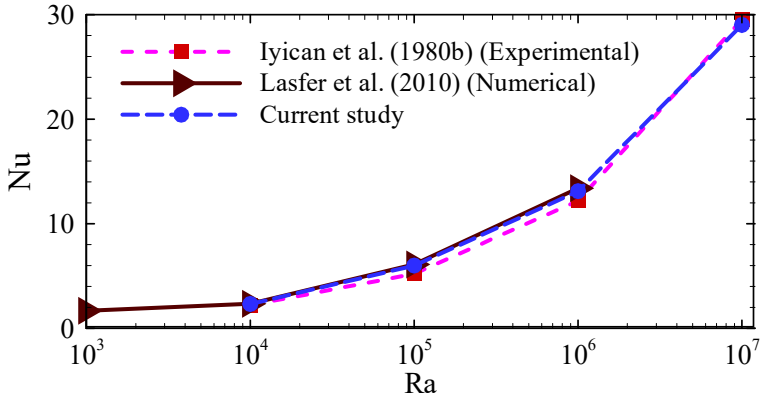

Figure 4. Quantitative comparison of the present findings with the experimental [35] and numerical [47] results for Nu at different Ra.

6. Results and Discussions

The validated numerical model is used to examine the transient NC, heat transfer (HT), and entropy generation (EG) within a stratified trapezoid-shaped cavity. The cavity is characterized by a heated bottom, a cooled top, and thermally stratified inclined walls. This research involved conducting 2D numerical simulations using a Pr of 7.01 and Ra spanning from 10 to 10^6, with an *AR* of 0.5. The numerical outcomes show that at lower Ra values, the flow is prevailed by conduction, whereas at higher Ra, a sequence of bifurcations happens, leading to a transition from a symmetric steady to a chaotic state.

6.1. Development of Symmetrical Flow

At the beginning, the bottom of the cavity is heated, the inclined walls are thermally stratified, and the top wall is cooled. As a result of the temperature variation along the internal surfaces, a thermal boundary layer develops on all interior surfaces, leading to the onset of primary circulation. The transitional flow is marked by the emergence of convective instabilities in the form of ascending or descending plumes and the development of cellular flow structure. For Ra values of 10 to 10^4, it is manifest that the flow development within the cavity is always symmetrical with respect to the cavity's *y*-axis, as shown in Figure 5. No descending or ascending plumes formed for the Rayleigh numbers of 10 to 10^3, and the flow is dominated by conduction. With a Ra of 10^4, two ascending plumes form within the cavity, but the flow is still dominated by conduction.

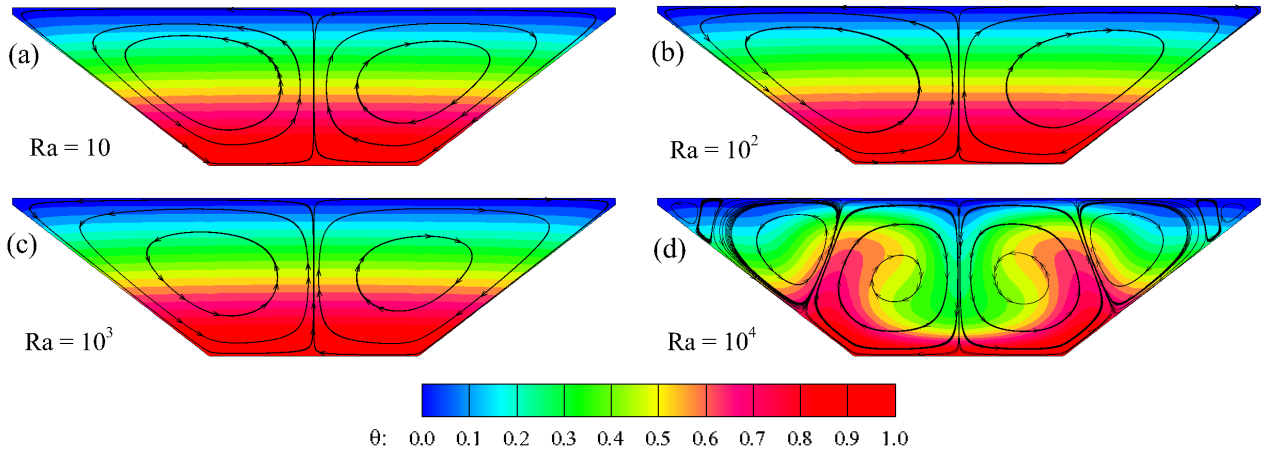

Figure 5. Flow development for lower Rayleigh numbers at the fully developed stage: (**a**) for Ra = 10, (**b**) for Ra = 10^2, (**c**) for Ra = 10^3, and (**d**) for Ra = 10^4.

6.2. Development of Asymmetrical Flow

For lower Ra spanning from 10 to 10^4, the flow remains symmetric with respect to the cavity's *y*-axis, as shown in Figure 5. To understand the asymmetrical flow, consider the streamlines and isotherms for Ra of 9×10^4 and 10^5. At the Rayleigh number of 9×10^4, the flow is undoubtedly symmetric, as portrayed in Figure 6a. However, at a Ra of 10^5, a more intense, frenetic flow pattern emerges, with two larger cells moving toward the center of the cavity from one side to the other, as illustrated in Figure 6b. At a Ra of 10^5, a pitchfork bifurcation occurs, sifting the flow from a symmetric to an asymmetric state. This demonstrates Rayleigh–Bénard instability.

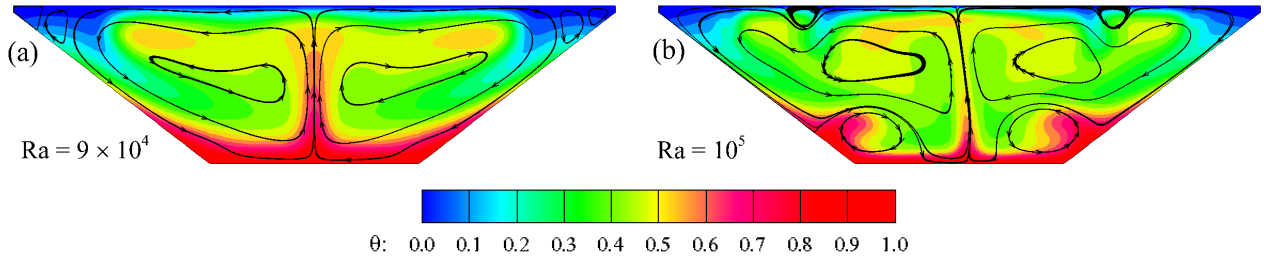

Figure 6. Observation of the pitchfork bifurcation using isotherm and streamline contours: (**a**) for symmetric state and (**b**) for asymmetric state.

For better understanding of the asymmetrical flow, consider the average Nusselt number (Nu) time series at the sloped walls. As depicted in Figure 7, the Nu time series at the left and right sloped walls coincide for an extended period at a Rayleigh number of 9×10^4, indicating a symmetrical flow relative to the cavity's mid-plane during that period. However, at a Rayleigh number of 10^5, the Nu time series deviates. In the interval of $\tau = 430$ to 500, this deviation confirms that a pitchfork bifurcation has happened, causing the flow to shift from a symmetric to an asymmetric state.

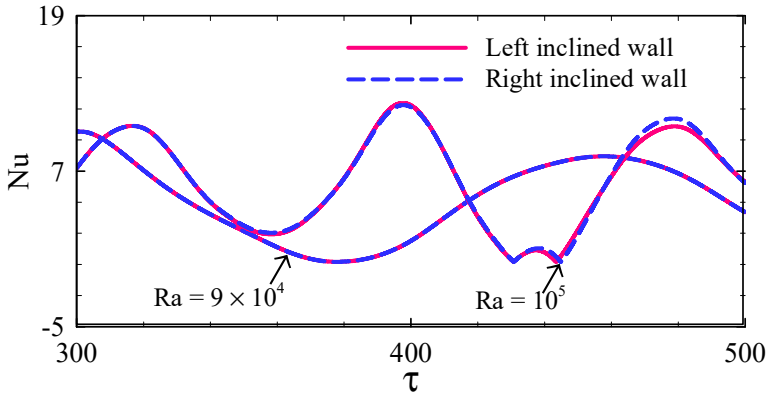

Figure 7. Nusselt number time series at the sloped walls to illustrate the pitchfork bifurcation.

6.3. Development of Unsteady Flow

Temperature time series (TTS) and their corresponding spectral analysis are analyzed for higher Ra at location P_2 (0, 0.40), as depicted in Figure 8, to show the transition from a steady state to chaos. At a Rayleigh number of 10^5, the flow is in a fully steady state throughout the fully developed stage (FDS), as portrayed in Figure 8a, while at a Rayleigh number of 2×10^5, the flow becomes periodic, as represented in Figure 8b. This indicates that a Hopf bifurcation occurs from a steady state to a periodic state between Rayleigh numbers of 10^5 and 2×10^5. Additionally, the spectral analysis of the TTS, depicted in Figure 8c,e, reveals that the flow fluctuates with harmonic modes, featuring a principal

peak frequency f_p of 0.145 and 0.488, which affirms the periodic flow for Rayleigh numbers of 2×10^5 and 4×10^5.

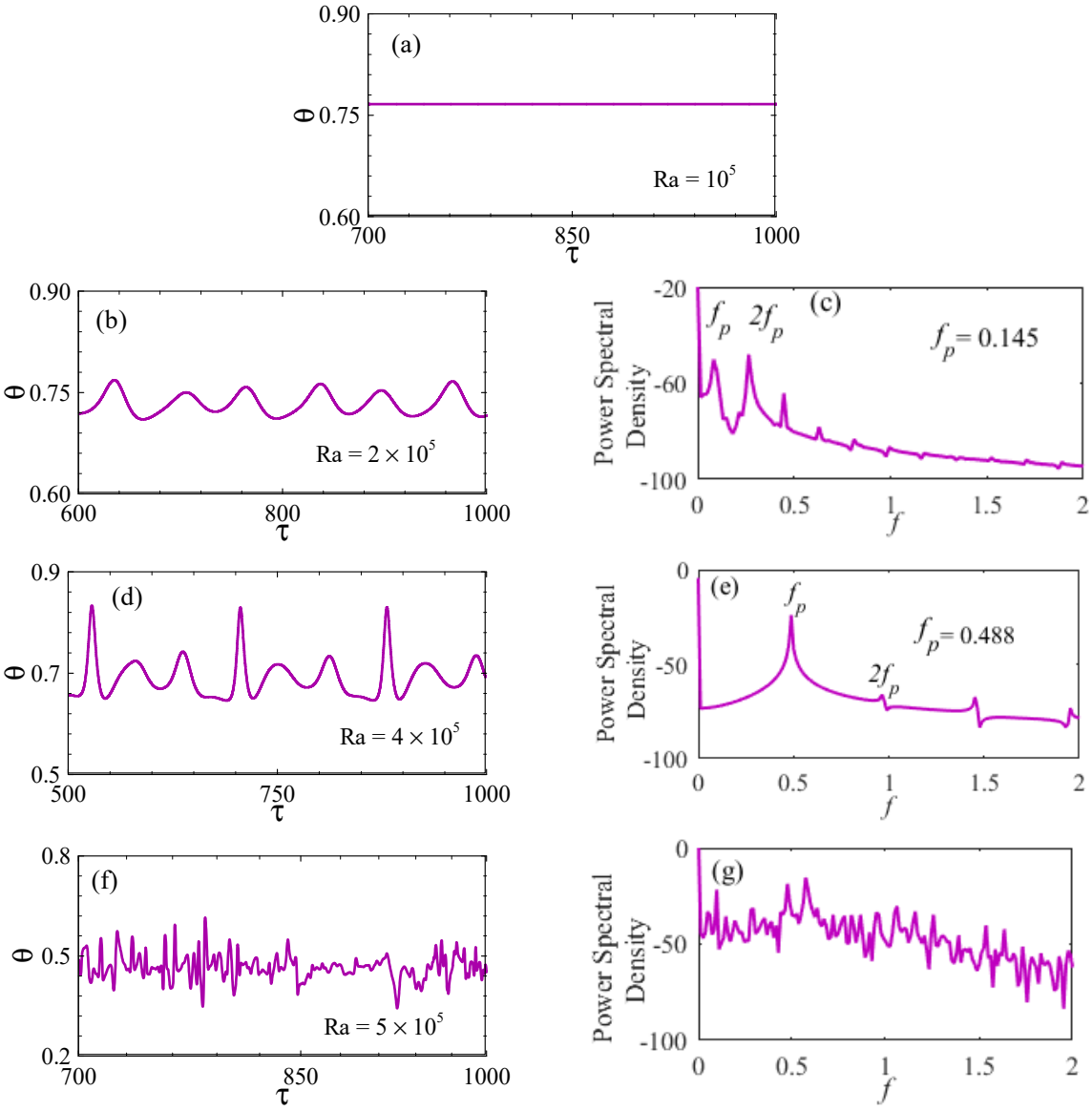

Figure 8. Time series of temperature and the corresponding spectral analysis in the FDS: (**a**) steady state for Ra = 10^5, (**b**,**c**) transition to periodic state for Ra = 2×10^5, (**d**,**e**) remains periodic for Ra = 4×10^5, and (**f**,**g**) transition to chaotic state for Ra = 5×10^5.

As Ra increases, the periodic flow patterns shift, as seen at Ra = 4×10^5 in Figure 8d. The periodic flow shifts to chaotic behavior at a Rayleigh number of 5×10^5. This indicates that another bifurcation occurs between Rayleigh numbers of 4×10^5 and 5×10^5, transitioning the flow from a periodic to a chaotic state. The spectral analysis shown in Figure 8g for Ra = 5×10^5 reveals that the principal peak frequency begins to fluctuate, and the subharmonic mode disappears, further confirming the transition from periodic to chaotic flow.

To comprehend the unsteady flow, consider the limit point and limit cycles at location P_3 (0, 0.67) on the v-θ plane over the time intervals τ = 500 and 1000. As portrayed in Figure 9a, for a Ra of 10^5, the trajectory approaches a fixed point (marked by a circular point). In contrast, Figure 9b displays the trajectory moving toward a closed limit cycle for a Rayleigh number of 2×10^5 (characterized by an orbit). The change from a fixed point to

a limit cycle attractor as the Rayleigh number increases from 10^5 to 2×10^5 suggests the development of a Hopf bifurcation. It is clear from Figure 9c that very similar limit cycles emerge, indicating the existence of periodic flows for Ra values of 4×10^5.

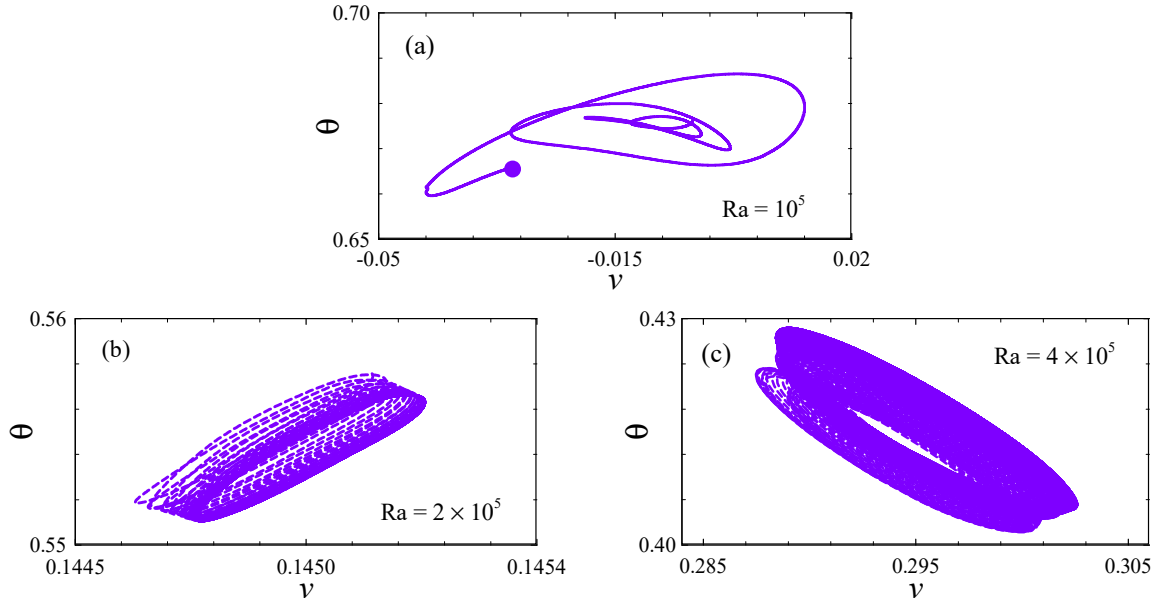

Figure 9. Limit point and limit cycles at location P_3 (0, 0.67): (**a**) for Ra = 10^5, (**b**) for Ra = 2×10^5, and (**c**) for Ra = 4×10^5.

The phase space trajectory in the v-θ planes at point P_3 (0, 0.67) is presented in Figure 10 for Rayleigh numbers of 2×10^5, 4×10^5, and 5×10^5 to provide further insight. In Figure 10a,b, the approximately identical limit cycles clearly indicate periodic flow at Rayleigh numbers of 2×10^5 and 4×10^5. In contrast, Figure 10c shows chaotic trajectories for Rayleigh numbers of 5×10^5. This suggests that another bifurcation occurs, marking the transition from periodic to chaotic states, between the Rayleigh numbers of 4×10^5 and 5×10^5.

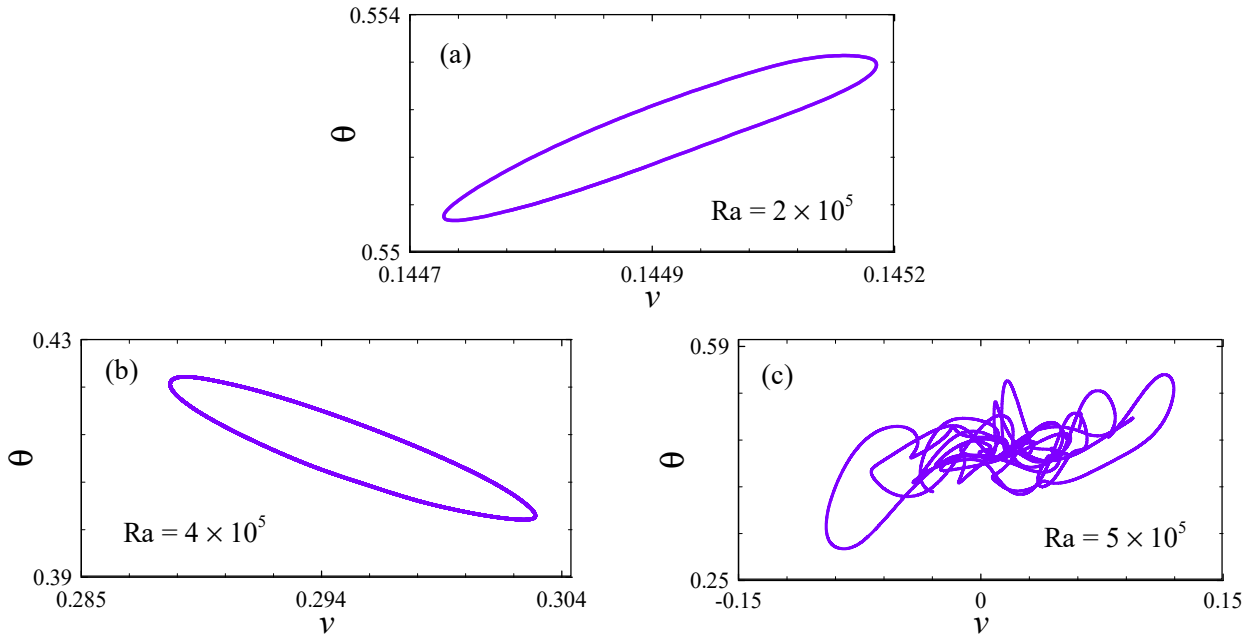

Figure 10. Phase space trajectory at location P_3 (0, 0.67): (**a**) for Ra = 2×10^5, (**b**) for Ra = 4×10^5, and (**c**) for Ra = 5×10^5.

6.4. Effects of Ra on Fluid Flow and EG

Figure 11 displays the variations in streamlines, isotherms, and entropy generation (EG) due to HT, EG due to FF, and local EG for Ra spanning from 10^5 to 10^6. The streamline and isotherm contours portrayed in Figure 11a represent the paths of fluid flow. At Ra = 10^5, three prominent vortices and four convective cells are formed within the cavity. The vortices are formed from the heated bottom wall. At the FDS, the flow reaches a steady state at Ra = 10^5. As Ra increases, the buoyancy force also increases, leading to more pronounced and stronger vortices adjacent to the bottom and the lower part of the sloped wall region. This indicates an increase in fluid circulation in this area. At Ra = 5×10^5, signifying a higher buoyancy force, the vortices shift their positions within the cavity. This suggests more complex flow behavior in the cavity as Ra reaches higher values. At Ra = 10^6, additional tiny cells form adjacent to the top wall, and non-uniform vortices are formed inside of the cavity. This indicates that the flow becomes more complicated, transitioning to chaotic behavior.

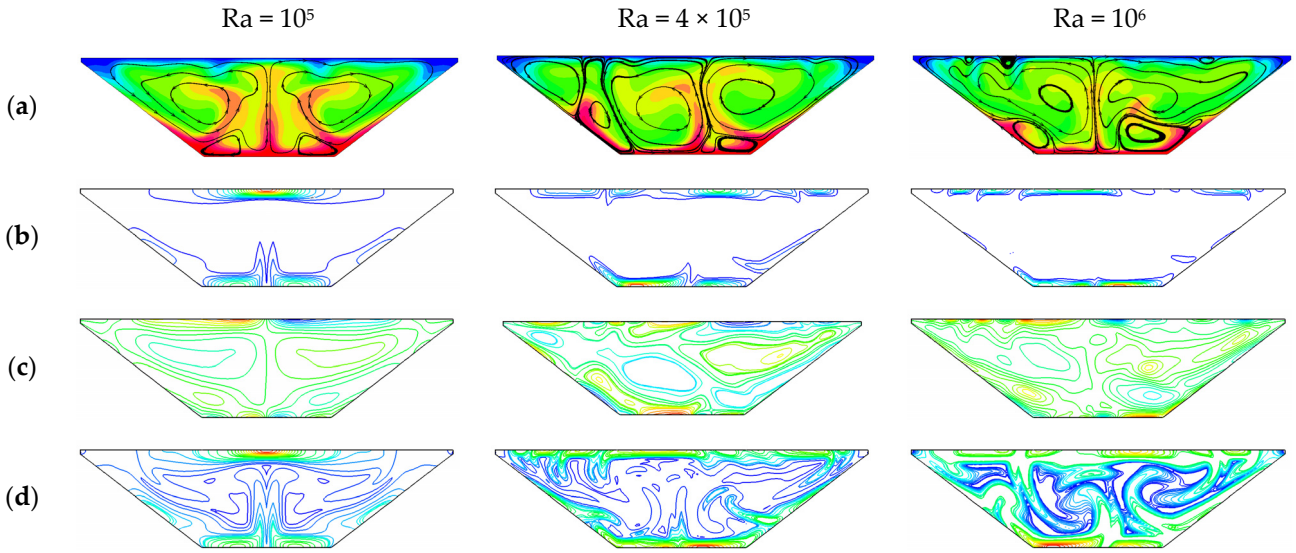

Figure 11. Distribution of (**a**) streamline and isotherms, (**b**) EG due to HT, (**c**) EG due to FF, and (**d**) local EG for different Rayleigh numbers.

At lower Ra values, EG due to HT is dominant over EG due to FF. Figure 11b,c illustrate that as Ra increases, EG due to HT decreases while EG due to FF increases within the cavity. This trend suggests that at higher Ra values, FF becomes a more significant contributor to EG compared with HT. When Ra increases and the buoyancy force become more robust, fluid motion becomes stronger, increasing FF. The relatively weak buoyancy forces at lower Ra result in less fluid motion and weaker FF effects, making HT a dominant factor in generating entropy. Figure 11d also reveals that local EG increases as Ra increases. Specifically, regions near the cooler top cold wall exhibit higher local EG values. This indicates that increasing Ra leads to higher EG associated with thermal losses in this area.

6.5. Variation of Average Bejan Number

The average Bejan number (Be_{avg}) is a non-dimensional number that qualitatively represents the ratio of the EG due to conduction HT to the total EG. In other words, it represents the contribution of the conduction HT to the total EG. Figure 12 illustrates the variation of Be_{avg} with the Ra. According to the figure, it is obvious that as Ra increases, Be_{avg} decreases. This is because at low Ra, conduction is the primary mode of HT, making the influence of the temperature gradient on total EG significant. As a consequence, Be_{avg} is near unity. As Ra increases, however, convection becomes the principal mode of HT, making

the influence of the temperature gradient on the total EG less significant. Additionally, strong convection currents generate local eddies, increasing local frictional resistance and leading to greater EG. At Ra values of 10^3 and 10^5, Be_{avg} is greater than 0.5, signifying that EG due to HT dominates over EG due to FF. However, at higher Ra values (5×10^5 and 10^6), Be_{avg} is lower than 0.5, indicating that EG due to FF is more significant than EG due to HT.

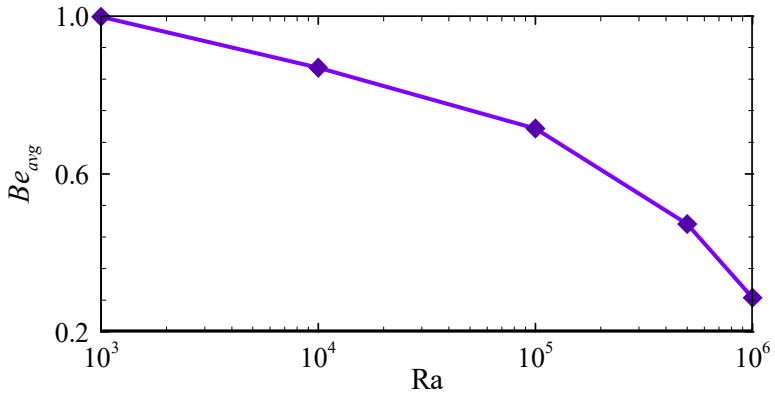

Figure 12. Changes in average Bejan number with Rayleigh numbers.

6.6. Heat Transfer

The isotherms and streamlines do not quantify the HT rate on the walls of the enclosure, but they offer insights into the flow structures and the factors that influence them. The Nu time series at the bottom and top walls are calculated and demonstrated in Figure 13. The cavity initially contains thermally stratified water, leading to temperature variations inside. Consequently, the temperatures of the water near the bottom, top, and inclined walls are equivalent to those of the walls themselves. Despite the enclosure having a heated bottom, a cooled top, and thermally stratified sloped walls, there is minimal temperature variation between the walls and the water near them due to the initial thermal stratification. This results in very low heat transfer from the walls, leading to minimal Nu. As the transitional stage begins, the stratification diminishes, and oscillations in Nu increase with the rising Rayleigh number. Because the convection becomes dominant, the Nu shows oscillatory behavior during the transitional stage for higher Rayleigh numbers. At the fully developed stage, the Nu becomes a steady state for Ra $\leq 10^5$, periodic for Ra = 2×10^5, and chaotic for Ra $\geq 5 \times 10^5$. These findings are compatible with those in Figures 9 and 10.

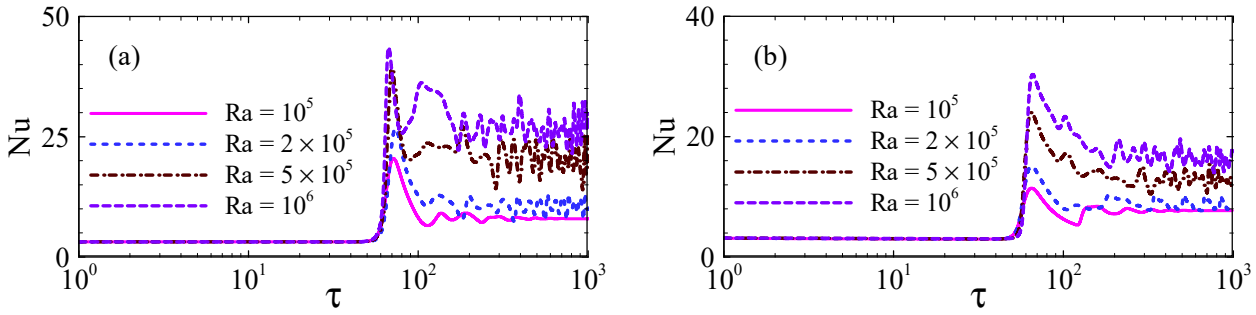

Figure 13. Nu time series at the horizontal walls for different Rayleigh numbers: (**a**) at the bottom wall and (**b**) at the top wall.

6.7. Variation of Nu, E_{avg}, and ECOP for Different Ra

Table 3 displays the discrepancy of Nu, E_{avg}, and the ecological coefficient of performance (ECOP) for various Ra. The rate of increment of the Nu and the E_{avg} with increasing Rayleigh numbers is not uniform. As the Ra value rises from 10^3 to 10^4, the rate of increase

in Nu is 45.58%, and in the E_{avg} it is 54.72%, whereas as Ra increases from 10^5 to 10^6, the Nu increases by 52.71% and the E_{avg} increases by 82.38%. This suggests that thermal transport is not linearly proportional to the Ra.

Table 3. Variation of Nu and E_{avg} for various Ra.

Ra	10^3	10^4	10^5	5×10^5	10^6
Nu	2.8299	5.2002	7.0909	11.9060	14.9935
E_{avg}	3.6043	7.9591	12.6171	42.2933	71.5994
ECOP	0.78515	0.65337	0.56201	0.28151	0.20941

As the Ra increases, both the Nu and the E_{avg} increase, while the ECOP declines. The highest ECOP value indicates that the cavity's energy efficiency increases and that environmental impact decreases. For Ra = 10^3, the cavity exhibits the highest ECOP; on the other hand, the lowest ECOP is seen for Ra = 10^6. We conclude that with the increase in Ra, there could be a decrease in ECOP values, signifying a possible decline in energy efficiency and an escalation of the environmental impact.

7. Conclusions

The present study examined the natural convection HT and EG analysis within a trapezoid-shaped cavity containing water with thermal stratification. The FV method was utilized to conduct the numerical simulation. An extensive range of Rayleigh numbers (10 to 10^6), an AR of 0.5, and a Pr of 7.01 for water were used for the numerical simulation. The pivotal findings of this study are as follows:

- In the beginning, the flow is marked by the development of thermal boundary layers along all internal surfaces and the onset of primary circulations. During the transitional stage, convective instabilities appear as rising and falling thermal plumes, leading to the construction of cellular flow patterns.
- The steady-state flow at Ra < 9×10^4 is marked by symmetric flow around the cavity's symmetrical plane.
- The shift of the flow from a symmetrical to an asymmetrical state due to pitchfork bifurcation occurs between the Rayleigh numbers of 9×10^4 and 10^5.
- The shift of the flow from an asymmetric steady state to a periodic state due to Hopf bifurcation occurs between the Rayleigh numbers of 10^5 and 2×10^5.
- The shift of the flow from a periodic to a chaotic state due to another bifurcation occurs between the Rayleigh numbers of 4×10^5 and 5×10^5.
- As Ra increases from 10^3 to 10^6, the rate of increment in Nu is 81.13%, and the average entropy generation is 94.97%.
- For the Ra values of 10^3 to 10^5, $Be_{avg} > 0.5$, signifying that EG due to HT dominates over EG due to FF. However, for higher Ra values of 5×10^5 to 10^6, $Be_{avg} < 0.5$, indicating that EG due to FF becomes more significant than EG due to HT.
- As the Ra value increases from 10^3 to 10^6, it results in a decrease in energy efficiency and an increased environmental impact.

8. Limitations and Future Works

The present study has focused exclusively on a two-dimensional problem. However, at higher Ra, three-dimensional effects may become significant, requiring three-dimensional direct numerical simulations (DNSs) on finer meshes. While this is beyond the scope of the current work, it represents a promising direction for future research.

For the thermally stratified water within the trapezoid cavity, a single Prandtl number (7.01) was chosen for the numerical simulation. Future research could expand on this work by examining an extensive range of Prandtl numbers.

Author Contributions: Conceptualization, S.C.S. and S.B.; methodology, M.M.R.; software, M.M.R.; validation, M.M.R. and S.B.; formal analysis, M.M.R., S.B. and S.C.S.; investigation, M.M.R. and S.B.; resources, M.M.R.; data curation, M.M.R.; writing—original draft preparation, M.M.R.; writing—review and editing, S.B. and S.C.S.; visualization, M.M.R.; supervision, S.B. and S.C.S.; project administration, S.B. All authors have read and agreed to the published version of the manuscript.

Funding: This research received no external funding.

Data Availability Statement: The original contributions presented in this study are included in the article. Further inquiries can be directed to the corresponding author(s).

Conflicts of Interest: The authors declare no conflicts of interest.

Nomenclature

AR	aspect ratio
L, H	half-length and height of the cavity (m)
g	gravitational force (m/s^2)
t	time (s)
Cp	specific heat (J/kg·K)
P	pressure (N/m^2)
p	dimensionless pressure
T	temperature (K)
T_∞	environmental temperature (K)
T_h	temperature of the bottom wall (K)
T_c	temperature of the top wall (K)
T_i	temperature of the inclined walls (K)
ΔT	temperature difference, $(T_h - T_c)$
Gr	Grashof number, $g\beta(T_h - T_c)H^3/\nu^2$
Pr	Prandtl number
E_{gen}	entropy generation
Ra	Rayleigh number, $g\beta(T_h - T_c)H^3/\nu\kappa$
Nu	Nusselt number
E_f	entropy generation due to fluid friction
E_l	local entropy generation
Nu$_{avg}$	average Nusselt number
E_{avg}	average entropy generation
Be_l	local Bejan number
Be_{avg}	average Bejan number
k	thermal conductivity (W/(m·K))
X, Y	coordinates
x, y	dimensionless coordinates
U, V	velocity components (m/s)
u, v	dimensionless velocity components

Greek symbols

κ	thermal diffusivity (m^2/s)
θ	dimensionless temperature
ν	kinematic viscosity (m^2/s)
ψ	irreversibility distribution ratio
φ	inclination angle
ρ	density (kg/m^3)
E_θ	entropy generation due to heat transfer
τ	dimensionless time
$\Delta\tau$	dimensionless time step
θ_i	dimensionless temperature of the inclined walls
θ_c	dimensionless temperature of the top wall
θ_h	dimensionless temperature of the bottom wall

References

1. Nourdanesh, N.; Hossainpour, S.; Adamiak, K. Numerical simulation and optimization of natural convection heat transfer enhancement in solar collectors using electrohydrodynamic conduction pump. *Appl. Therm. Eng.* **2020**, *180*, 115825.
2. Letan, R.; Dubovsky, V.; Ziskind, G. Passive ventilation and heating by natural convection in a multi-storey building. *Build. Environ.* **2003**, *38*, 197–208.
3. Chen, H.T.; Hsieh, Y.L.; Chen, P.C.; Lin, Y.F.; Liu, K.C. Numerical simulation of natural convection heat transfer for annular elliptical finned tube heat exchanger with experimental data. *Int. J. Heat Mass Transf.* **2018**, *127*, 541–554.
4. Rath, S.; Dash, S.K. Thermal performance of a wavy annular finned horizontal cylinder in natural convection for electronic cooling application. *Int. Commun. Heat Mass Transf.* **2021**, *128*, 105623.
5. Vogel, J.; Felbinger, J.; Johnson, M. Natural convection in high temperature flat plate latent heat thermal energy storage systems. *Appl. Energy* **2016**, *184*, 184–196.

6. Bhavsar, H.P.; Patel, C.M. Performance investigation of natural and forced convection cabinet solar dryer for ginger drying. *Mater. Today Proc.* **2021**, *47*, 6128–6133.
7. Saha, S.C. Unsteady natural convection in a triangular enclosure under isothermal heating. *Energy Build.* **2011**, *43*, 695–703. [CrossRef]
8. Bhowmick, S.; Saha, S.C.; Qiao, M.; Xu, F. Transition to a chaotic flow in a V-shaped triangular cavity heated from below. *Int. J. Heat Mass Transf.* **2019**, *128*, 76–86.
9. Wang, X.; Bhowmick, S.; Tian, Z.F.; Saha, S.C.; Xu, F. Experimental study of natural convection in a V-shape-section cavity. *Phys. Fluids* **2021**, *33*, 014104. [CrossRef]
10. Bhowmick, S.; Xu, F.; Molla, M.M.; Saha, S.C. Chaotic phenomena of natural convection for water in a V-shaped enclosure. *Int. J. Therm. Sci.* **2022**, *176*, 107526.
11. Chen, C.C.; Eichhorn, R. Natural convection from a vertical surface to a thermally stratified fluid. *ASME J. Heat Transf.* **1976**, *98*, 446–451. [CrossRef]
12. Chen, C.C.; Eichhorn, R. *Natural Convection from Simple Bodies Immersed in Thermally Stratified Fluids*; Report No. UKY TR 105-ME 14-77; ORES Publications, College of Engineering, University of Kentucky Lexington: Lexington, KY, USA, 1977.
13. Eichhorn, R. Natural convection in a thermally stratified fluid. *Prog. Heat Mass Transf.* **1969**, *2*, 41–53.
14. Eichhorn, R.; Lienhard, J.H.; Chen, C.C. Natural convection from isothermal spheres and cylinders immersed in a stratified fluid. In *International Heat Transfer Conference Digital Library*; Begel House Inc.: Danbury, CT, USA, 1974.
15. Angirasa, D.; Peterson, G.P. Natural convection heat transfer from an isothermal vertical surface to a fluid saturated thermally stratified porous medium. *Int. J. Heat Mass Transf.* **1997**, *40*, 4329–4335. [CrossRef]
16. Tripathi, R.K.; Nath, G. Unsteady natural convection flow over a vertical plate embedded in a stratified medium. *Int. J. Heat Mass Transf.* **1993**, *36*, 1125–1128. [CrossRef]
17. Hossain, M.A.; Paul, S.C.; Mandal, A.C. Natural convection flow along a vertical circular cone with uniform surface temperature and surface heat flux in a thermally stratified medium. *Int. J. Numer. Methods Heat Fluid Flow* **2002**, *12*, 290–305. [CrossRef]
18. Lin, W.; Armfield, S.W.; Morgan, P.L. Unsteady natural convection boundary-layer flow along a vertical isothermal plate in a linearly stratified fluid with Pr > 1. *Int. J. Heat Mass Transf.* **2002**, *45*, 451–459. [CrossRef]
19. Shapiro, A.; Fedorovich, E. Prandtl number dependence of unsteady natural convection along a vertical plate in a stably stratified fluid. *Int. J. Heat Mass Transf.* **2004**, *47*, 4911–4927. [CrossRef]
20. Shapiro, A.; Fedorovich, E. Unsteady convectively driven flow along a vertical plate immersed in a stably stratified fluid. *J. Fluid Mech.* **2004**, *498*, 333–352. [CrossRef]
21. Shapiro, A.; Fedorovich, E. Natural convection in a stably stratified fluid along vertical plates and cylinders with temporally periodic surface temperature variations. *J. Fluid Mech.* **2006**, *546*, 295–311. [CrossRef]
22. Patterson, J.; Imberger, J. Unsteady natural convection in a rectangular cavity. *J. Fluid Mech.* **1980**, *100*, 65–86. [CrossRef]
23. Kuhn, D.; Oosthuizen, P.H. Unsteady natural convection in a partially heated rectangular cavity. *J. Heat Transf.* **1987**, *109*, 798–801. [CrossRef]
24. Lei, C.; Armfield, S.W.; Patterson, J.C. Unsteady natural convection in a water-filled isosceles triangular enclosure heated from below. *Int. J. Heat Mass Transf.* **2008**, *51*, 2637–2650.
25. Ma, J.; Xu, F. Unsteady natural convection and heat transfer in a differentially heated cavity with a fin for high Rayleigh numbers. *Appl. Therm. Eng.* **2016**, *99*, 625–634. [CrossRef]
26. Xu, F.; Patterson, J.C.; Lei, C. Unsteady flow and heat transfer adjacent to the sidewall wall of a differentially heated cavity with a conducting and an adiabatic fin. *Int. J. Heat Fluid Flow* **2011**, *32*, 680–687.
27. Elkhazen, M.I.; Hassen, W.; Gannoun, R.; Hussein, A.K.; Borjini, M.N. Numerical study of electroconvection in a dielectric layer between two cofocal elliptical cylinders subjected to unipolar injection. *J. Eng. Phys. Thermophys.* **2019**, *92*, 1318–1329.
28. Elkhazen, M.I.; Hassen, W.; Kolsi, L.; Oztop, H.F.; Al-Rashed, A.A.; Borjini, M.N.; Abu-Hamdeh, N. Heat transfer intensification induced by electrically generated convection between two elliptical cylinders. *Int. J. Therm. Sci.* **2019**, *135*, 523–532.
29. Hassen, W.; Elkhazen, M.I.; Traore, P.; Borjini, M.N. Numerical study of the electro–thermo-convection in an annular dielectric layer subjected to a partial unipolar injection. *Int. J. Heat Fluid Flow* **2014**, *50*, 201–208.
30. Rejeb, S.; Hassen, W.; Kolsi, L.; Estellé, P. Heat transfer by oil natural convection in an annular space under combined effects of carbon nanotubes and electric field. *Int. Commun. Heat Mass Transf.* **2022**, *138*, 106345. [CrossRef]
31. Hassen, W.; Elkhazen, M.I.; Traore, P.; Borjini, M.N. Charge injection in horizontal eccentric annuli filled with a dielectric liquid. *Eur. J. Mech.-B/Fluids* **2018**, *72*, 691–700.
32. Elkhazen, M.I.; Hassen, W.; Öztop, H.F.; Kolsi, L.; Al-Rashed, A.A.; Borjini, M.N.; Ali, M.E. Electro-thermo-convection in dielectric liquid subjected to partial unipolar injection between two eccentric cylinders. *Int. J. Numer. Methods Heat Fluid Flow* **2019**, *29*, 78–93.
33. Akrour, D.; Elkhazen, M.I.; Hassen, W.; Kriaa, K.; Maatki, C.; Hadrich, B.; Kolsi, L. Numerical Investigation of the Electro-Thermo Convection in an Inclined Cavity Filled with a Dielectric Fluid. *Processes* **2023**, *11*, 2506. [CrossRef]

34. Iyican, L.; Bayazitoglu, Y.; Witte, L.C. An analytical study of natural convective heat transfer within a trapezoidal enclosure. *J. Heat Transf.* **1980**, *102*, 640–647.
35. Iyican, L.; Witte, L.C.; Bayazitoglu, Y. An experimental study of natural convection in trapezoidal enclosures. *J. Heat Transf.* **1980**, *102*, 648–653.
36. Lam, S.W.; Gani, R.; Symons, J.G. Experimental and numerical studies of natural convection in trapezoidal cavities. *J. Heat Transf.* **1989**, *111*, 372–377. [CrossRef]
37. Lee, T.S. Numerical experiments with fluid convection in tilted nonrectangular enclosures. *Numer. Heat Transf. Part A Appl.* **1991**, *19*, 487–499.
38. Perić, M. Natural convection in trapezoidal cavities. *Numer. Heat Transf. Part A Appl.* **1993**, *24*, 213–219.
39. Kuyper, R.A.; Hoogendoorn, C.J. Laminar natural convection flow in trapezoidal enclosures. *Numer. Heat Transf. Part A Appl.* **1995**, *28*, 55–67. [CrossRef]
40. Moukalled, F.; Darwish, M. Natural convection in a partitioned trapezoidal cavity heated from the side. *Numer. Heat Transf. Part A Appl.* **2003**, *43*, 543–563.
41. Moukalled, F.; Darwish, M. Natural convection in a trapezoidal enclosure heated from the side with a baffle mounted on its upper inclined surface. *Heat Transf. Eng.* **2004**, *25*, 80–93.
42. Moukalled, F.; Darwish, M. Buoyancy-induced heat transfer in a trapezoidal enclosure with offset baffles. *Numer. Heat Transf. Part A Appl.* **2007**, *52*, 337–355.
43. Natarajan, E.; Roy, S.; Basak, T. Effect of various thermal boundary conditions on natural convection in a trapezoidal cavity with linearly heated side wall (s). *Numer. Heat Transf. Part B Fundam.* **2007**, *52*, 551–568.
44. Natarajan, E.; Basak, T.; Roy, S. Natural convection flows in a trapezoidal enclosure with uniform and non-uniform heating of bottom wall. *Int. J. Heat Mass Transf.* **2008**, *51*, 747–756.
45. Basak, T.; Roy, S.; Pop, I. Heat flow analysis for natural convection within trapezoidal enclosures based on heatline concept. *Int. J. Heat Mass Transf.* **2009**, *52*, 2471–2483.
46. Basak, T.; Roy, S.; Singh, A.; Pandey, B.D. Natural convection flow simulation for various angles in a trapezoidal enclosure with linearly heated side wall (s). *Int. J. Heat Mass Transf.* **2009**, *52*, 4413–4425.
47. Lasfer, K.; Bouzaiane, M.; Lili, T. Numerical study of laminar natural convection in a side-heated trapezoidal cavity at various inclined heated sidewalls. *Heat Transf. Eng.* **2010**, *31*, 362–373.
48. Rahaman, M.M.; Titab, R.; Bhowmick, S.; Mondal, R.N.; Saha, S.C. Unsteady 2D flow in an initially stratified air-filled trapezoid. *Jagannath Univ. J. Sci.* **2022**, *8*, 1–6.
49. Rahaman, M.M.; Bhowmick, S.; Mondal, R.N.; Saha, S.C. Unsteady natural convection in an initially stratified air-filled trapezoidal enclosure heated from below. *Processes* **2022**, *10*, 1383. [CrossRef]
50. Rahaman, M.M.; Bhowmick, S.; Mondal, R.N.; Saha, S.C. A Computational Study of Chaotic Flow and Heat Transfer within a Trapezoidal Cavity. *Energies* **2023**, *16*, 5031. [CrossRef]
51. Rahaman, M.M.; Bhowmick, S.; Mondal, R.N.; Saha, S.C. Transient 2D Flow in a Stratified Air-Filled Trapezoidal Cavity. 2024. Available online: https://papers.ssrn.com/sol3/papers.cfm?abstract_id=4874263 (accessed on 12 February 2025).
52. Rahaman, M.M.; Bhowmick, S.; Mondal, R.N.; Saha, S.C. Unsteady Natural Convection Flow Within a Trapezoidal Enclosure. 2024. Available online: https://papers.ssrn.com/sol3/papers.cfm?abstract_id=4951897 (accessed on 12 February 2025).
53. Bejan, A. Second law analysis in heat transfer. *Energy* **1980**, *5*, 720–732.
54. Bejan, A. Entropy generation minimization: The new thermodynamics of finite-size devices and finite-time processes. *J. Appl. Phys.* **1996**, *79*, 1191–1218.
55. Biswal, P.; Basak, T. Entropy generation vs energy efficiency for natural convection based energy flow in enclosures and various applications: A review. *Renew. Sustain. Energy Rev.* **2017**, *80*, 1412–1457.
56. Goh, L.H.K.; Hung, Y.M.; Chen, G.M.; Tso, C.P. Entropy generation analysis of turbulent convection in a heat exchanger with self-rotating turbulator inserts. *Int. J. Therm. Sci.* **2021**, *160*, 106652.
57. Magherbi, M.; Abbassi, H.; Brahim, A.B. Entropy generation at the onset of natural convection. *Int. J. Heat Mass Transf.* **2003**, *46*, 3441–3450.
58. Ilis, G.G.; Mobedi, M.; Sunden, B. Effect of aspect ratio on entropy generation in a rectangular cavity with differentially heated vertical walls. *Int. Commun. Heat Mass Transf.* **2008**, *35*, 696–703.
59. Varol, Y.; Oztop, H.F.; Koca, A. Entropy generation due to conjugate natural convection in enclosures bounded by vertical solid walls with different thicknesses. *Int. Commun. Heat Mass Transf.* **2008**, *35*, 648–656.
60. Varol, Y.; Oztop, H.F.; Pop, I. Entropy generation due to natural convection in non-uniformly heated porous isosceles triangular enclosures at different positions. *Int. J. Heat Mass Transf.* **2009**, *52*, 1193–1205.
61. Basak, T.; Kaluri, R.S.; Balakrishnan, A.R. Entropy generation during natural convection in a porous cavity: Effect of thermal boundary conditions. *Numer. Heat Transf. Part A Appl.* **2012**, *62*, 336–364.

62. Siavashi, M.; Yousofv, R.; Rezanejad, S. Nanofluid and porous fins effect on natural convection and entropy generation of flow inside a cavity. *Adv. Powder Technol.* **2018**, *29*, 142–156.
63. Rahaman, M.M.; Bhowmick, S.; Saha, G.; Xu, F.; Saha, S.C. Transition to chaotic flow, bifurcation, and entropy generation analysis inside a stratified trapezoidal enclosure for varying aspect ratio. *Chin. J. Phys.* **2024**, *91*, 867–882.
64. Saha, S.C.; Patterson, J.C.; Lei, C. Natural convection and heat transfer in attics subject to periodic thermal forcing. *Int. J. Therm. Sci.* **2010**, *49*, 1899–1910.
65. Rahaman, M.M.; Bhowmick, S.; Ghosh, B.P.; Xu, F.; Mondal, R.N.; Saha, S.C. Transient natural convection flows and heat transfer in a thermally stratified air-filled trapezoidal cavity. *Therm. Sci. Eng. Prog.* **2024**, *47*, 102377.
66. Saha, S.C.; Gu, Y. Natural convection in a triangular enclosure heated from below and non-uniformly cooled from top. *Int. J. Heat Mass Transf.* **2015**, *80*, 529–538.

Disclaimer/Publisher's Note: The statements, opinions and data contained in all publications are solely those of the individual author(s) and contributor(s) and not of MDPI and/or the editor(s). MDPI and/or the editor(s) disclaim responsibility for any injury to people or property resulting from any ideas, methods, instructions or products referred to in the content.